An RC snubber design method to achieve optimized switching noise-loss trade-off of cascode GaN HEMTs

Xue, Peng; Hoene, Eckart; Davari, Pooya

Published in:
IET Power Electronics

DOI (link to publication from Publisher):
10.1049/pel2.12741

Publication date:
2024

Document Version
Accepted author manuscript, peer reviewed version

An RC Snubber Design Method to Achieve Optimized Switching Noise-Loss Trade-off of Cascode GaN HEMTs

Peng Xue, Eckart Hoene and Pooya Davari

***Abstract*—The cascode gallium nitride high electron mobility transistors (GaN HEMTs) are very vulnerable to self-sustained turn-off oscillation due to their cascode configuration. This paper presents a design approach for the RC snubber of cascode GaN HEMTs to achieve the optimized noise-loss trade-off. At first, an analytical model is proposed to describe the instability of cascode GaN HEMTs-based test circuits utilizing RC snubber. Based on the model, an analytical approach is proposed to achieve two optimum RC snubber designs S1 and S2. The design S1 can satisfactorily dampen the oscillation with minimum switching losses. The design S2 achieves maximum effective damping on the oscillation at a minimized cost of additional power losses. In the end, the accuracy of the proposed model is validated by the double-pulse test and good agreement is obtained.**

I. Introduction

The gallium nitride high electron mobility transistors (GaN HEMTs) become a promising candidate for next-generation power semiconductor devices. Thanks to the excellent properties of GaN material, the GaN HEMTs can achieve a much lower static state resistance and higher switching speed compared to the silicon-based counterparts [1]. As one of the solution for the normally-off GaN HEMTs, the cascode GaN HEMTs can achieve a very high turn-off speed. The merit makes the cascode GaN HEMTs a good candidate for high-efficiency power conversion applications.

The cascode GaN HEMTs has a major drawback, which is well-known as self-sustained turn-off oscillation [2]–[7]. Unlike the self-sustained oscillation of SiC MOSFET, which occurrence requires unrealistically large circuit stray inductances [8]–[10], the self-sustained turn-off oscillation of cascode GaN HEMTs can be triggered at a normal circuit setup [2]. Due to the cascode configuration, the internal gate loop of the LV MOSFET forms an LC resonant tank lacking effective damping and is prone to resonate with the power loop [2], [6], [11]. Under high current and voltage operation conditions, the turn-off oscillation can maintain self-sustaining because of the LC tank resonance [2], [4]. Fig. 1b shows the turn-off oscillation of cascode GaN HEMTs without using RC snubber. The self-sustained oscillation acts as a noise source in the power electronic systems, which generates severe electromagnetic interference (EMI) noise and disrupt the converter operation [12], [13]. In the worst-case scenario, the unstable oscillation can even induce the failure of the device [14], [15]. Therefore, an approach which can suppress the turn-off oscillation of cascode GaN HEMTs is vital to unlock the full potential of the device so that they can be used in the next generation of power

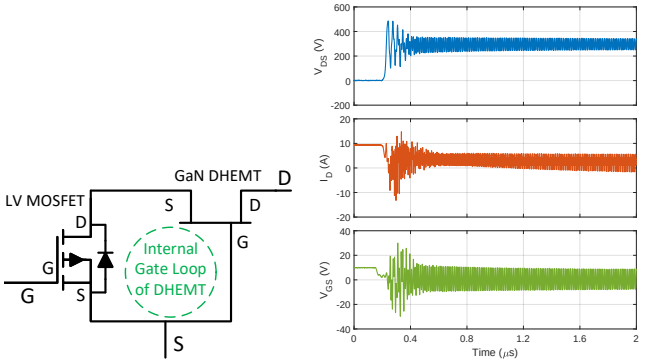

Fig. 1. The unstable turn-off oscillation of Cascode GaN HEMTs: (a) nderdamped gate loop of the GaN DHEMTs. (b) experimental 300V/10A turn-off waveforms without using RC snubber.

electronic applications. To suppress the self-sustained turn-off oscillation, various methods are proposed. In [2], the pivotal stray elements of cascode GaN HEMTs which can excite the turn-off oscillation are identified. A method is thereby proposed to optimize the pivotal stray elements so that the turn-off oscillation can be mitigated. However, the mitigation method is mainly for the device manufacturers and is not feasible for the power electronics engineers. In [16]–[19], it is also shown that the ferrite beads can be used to suppress the turn-off oscillation. However, the utilization of the ferrite beads also introduces additional stray elements in the circuit. If improper ferrite beads are utilized, the stray elements can induce extra oscillation [19].

As one of the most readily applicable approaches, resistor-capacitor (RC) snubber can be used to effectively suppress the self-sustained turn-off oscillation of cascode GaN HEMTs. However, to use the RC snubber, an appropriate snubber resistor and capacitor should be designed. In general, the RC snubber is designed to achieve maximum effective damping on the oscillation [20]–[22]. However, this kind of snubber design can greatly slow down the switching speed of GaN devices and induce massive switching losses. When the GaN devices operate under high-frequency conditions, this snubber design may not be the best choice since it can greatly reduce the efficiency of the power conversion system [23]–[25]. Therefore, it is also necessary to identify an optimum snubber design which can provide satisfactory effective damping with minimized switching losses.

Looking into the previous research on the RC snubber design method, most of them [20]–[28] are for non-cascode devices like GaN enhanced-mode HEMTs (EHEMTs) and SiC MOSFETs. The turn-off oscillation of GaN EHEMTs is mainly due to its reverse conduction characteristics [29], which can generate a positive feedback mechanism to excite the self-sustained oscillation The turn-off oscillation of SiC MOSFETs are related to the $C_{GD}dV/dt$ induced false turn-on of low-side MOSFET [9]. Due to the $C_{GD}dV/dt$ induced feedback, the low-side switch can turn off and on, which generates the oscillation [8]. Unlike these devices, cascode GaN HEMTs do not have the reverse condition characteristics like the GaN EHEMTs and false turn-on of SiC MOSFETs. Their oscillatory behaviour is mainly due to the cascode structure [2], [6], [11]. Since the cascode structure is not considered in the design, the RC snubber design methods are not applicable to the cascode GaN HEMTs. The papers [14], [16] report that the turn-off oscillation of cascode GaN HEMTs can be suppressed if a proper RC snubber design is utilized. However, the RC snubber design method which can achieve the best effective damping is not mentioned. In [30], an RC snubber design with a few Nano farads of snubber capacitor is utilized to suppress the turn-off oscillation of cascode GaN HEMTs. However, the extremely large snubber capacitor jeopardizes the benefits of low switching losses of cascode GaN HEMTs and thereby is not a good snubber design. Therefore, it is necessary to develop a method to identify the appropriate snubber designs for the cascode GaN HEMTs which can achieve optimum noise-loss trade-off.

The goal of this paper is to propose a new RC snubber design method for the cascode GaN HEMTs. Since the resonance between the underdamped internal gate loop of GaN DHEMT and power loop causes the oscillation of cascode GaN HEMTs, the RC snubber should be designed to suppress the resonance. Moreover, since the RC snubber generates additional power losses, the optimum RC snubber design methods should be considered to achieve the optimum noise-loss trade-off. The remainder of this paper is structured as follows. In section II, the impact of the RC snubber on the turn-off oscillation of cascode GaN HEMTs is analysed. Based on the analysis, an analytical model is proposed in section III to obtain the transfer function of the cascode GaN HEMTs-based test circuit utilizing RC snubber. The transfer function is analysed in section IV, which identifies the dominated conjugate pole pairs of the oscillatory system. In section V, an optimum RC snubber design method is proposed for the cascode GaN HEMTs-based circuit. In section VI, the design method is experimentally validated. In the end, the noise-loss trade-off of the proposed designs are compared with various other RC snubber designs.

II. The Impact of RC Snubber on the Turn-Off Oscillation of Cascode GaN HEMTs

Fig. 2 shows an equivalent schematic of the cascode GaN HEMTs-based test circuit utilizing RC snubber. In the circuit, T_1 is the cascode GaN HEMT under test. D_2 is the high-side freewheeling diode. L_0 is the load inductor. V_{DC} is the DC-bus voltage. R_G is the external gate resistance. V_{gg} is the gate drive voltage. L_C is the circuit stray inductance. L_G is the gate loop inductance. L_D is drain-side stray inductance. L_S is common source stray inductance. $L_{int1(2,3)}$ are the stray inductances of the bond wire interconnections between the LV MOSFET and DHEMT. R_{GH} is the internal gate resistance of the DHEMT. $C_{GD1(2)}$, $C_{DS1(2)}$ and $C_{GS1(2)}$ are the gate-drain, drain-source and gate-source capacitances of the LV MOSFET and DHEMT. R_{SN} and C_{SN} are the snubber resistor and capacitor.

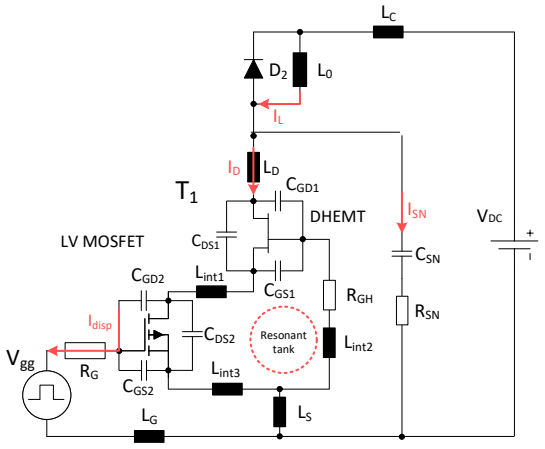

Fig. 2. Equivalent schematic of cascode GaN HEMTs based test circuit utilizing RC snubber.

Without utilizing the RC snubber, the occurrence of self-sustained turn-off oscillation of cascode GaN HEMTs requires two prerequisites [2]:

Firstly, at turn-off transient, high dV/dt is applied on the device, which generates displacement currents I_{disp} on C_{GD2}, as shown in Fig. 2. The I_{disp} generates a false triggering pulse, which reopens the LV MOSFET and causes the initial false turn-on.

Secondly, in the gate loop of DHEMTs, bond wire stray inductances $L_{int1(2,3)}$, gate resistance R_{GH} and device stray capacitances form a resonant tank, as shown in Fig. 2. In the cascode GaN HEMTs, the resistance R_{GH} is designed to be very small to achieve high switching speed and avoid some reliability problems [3]. The resonant tank thereby lacks effective damping [6], which can resonate with the power loop and make the oscillatory system very unstable. When the false turn-on occurs, a positive feedback mechanism is generated, which draws additional energy from the power supply and support turn-off oscillation to maintain self-sustaining [2].

The first prerequisite triggers the onset of self-sustained oscillation. The second condition determines whether the oscillation can maintain self-sustaining.

With RC snubber utilized in the test circuit, the RC snubber can mitigate the oscillation due to the following reasons:

Firstly, a part of drain current I_D is shared by the capacitance charging current I_{SN} on C_{SN}. The I_D thereby greatly reduces. At turn-off transient, the I_D is mainly supported by the CdV/dt induced displacement current on the device output capacitance. The reduction of I_D causes a great reduction of dV/dt, which can avoid the occurrence of the false turn-on.

Secondly, the RC snubber provides an additional path for the power loop oscillating current, which is damped by the snubber resistor. Due to the damping effect, the oscillatory system becomes more stable. If a proper RC snubber design is used, the oscillation can be suppressed.

It should be noticed that the second reason determines whether the RC snubber can suppress the turn-off oscillation. If the oscillatory system is very stable, the turn-off oscillation is suppressed even the false turn-on occurs. In this paper, the system instability of the circuit presented in Fig. 2 is analysed to identify the optimum design of RC snubber.

III. Analytical model of cascode GaN HEMTs Based Test Circuit Utilizing RC Snubber

In this section, an analytical model is proposed to analyse the instability of the cascode GaN HEMTs-based test circuit utilizing RC snubber. To analyse the circuit instability, it is necessary to convert the test circuit presented in Fig. 2 to its equivalent small-signal model. Fig. 3a shows the small-signal model of the test circuit presented in Fig. 2. In the model, the V_{DC} is short-circuited. The load inductor L_0 is open-circuited. Since the high-side freewheeling diode D_2 operates under on-state conditions, D_2 is thereby replaced as its on-state resistance R_{d2}. i_{H1} is the small-signal model of DHEMT's channel current. During the turn-off transient, the LV MOSFET first turn-off, and the LV MOSFET thereby operates under off-state. The turn-off of LV MOSFET thereby causes the turn-off of the channel current. To compensate for the channel current reduction, the drain-source voltage of the DHEMT greatly increase, which causes the turn-off oscillation. Therefore, the turn-off oscillation is excited by the channel current turn-off.

In [2], [11], [31], [32], it is widely proven that the circuit elements in the gate branch of the LV MOSFET have a very weak impact on the switching oscillation. The oscillation can still be self-sustained even the gate loop resonance is suppressed using ferrite beads [19]. This is because the unstable oscillatory system is mainly due to the underdamped resonant tank in the gate loop of DHEMTs, as shown in Fig. 2. During the oscillatory transient, the oscillating current mainly flows in the resonant tank and a very small component can flow to the gate branch of the LV MOSFET. Therefore, the gate branch has a minor impact on the oscillatory system and can thereby be neglected. With the gate branch removed, a simplified small-signal model is thereby can be obtained, as shown in Fig. 3b. In the model, the stray inductances $L_{DS} = L_D + L_S$ and $L_{int4} = L_{int1} + L_{int3}$. The stray capacitance $C_{OSS2} = C_{GD2} + C_{DS2}$. Based on the small-signal model, the following equations can be obtained:

$$v_{DS1} - v_{GS1} + sL_D i_{D1} - i_{G1}R_{GH} - sL_{int2}i_{G1} - R_{SN}i_S - v_{SN} = 0 \quad (1)$$

$$i_{D1} = sC_{DS1}v_{DS1} + sC_{GD1}(v_{DS1} - v_{GS1}) + i_{H1} \quad (2)$$

$$i_{G1} = sC_{GS1}v_{GS1} + sC_{GD1}(v_{GS1} - v_{DS1}) \quad (3)$$

$$i_{SN} = sC_{SN}v_{SN} \quad (4)$$

$$i_{D2} = sC_{OSS2}v_{DS2} \quad (5)$$

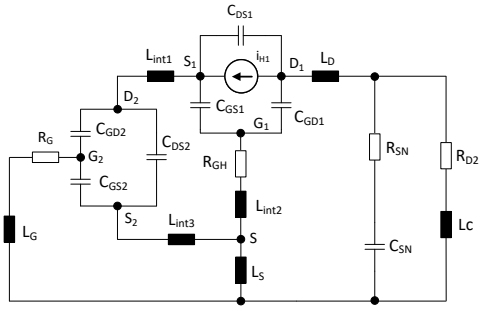

(a) Small-signal model.

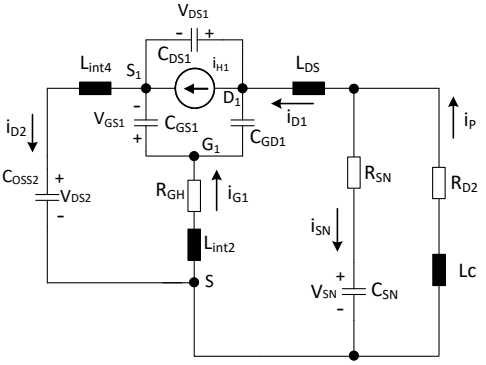

(b) Simplified small-signal model.

Fig. 3. Small-signal model of test circuit presented in Fig. 2. (a) Equivalent small-signal model, (b) Simplified small-signal model.

$$i_P = i_{SN} + i_{D1} \quad (6)$$

$$i_{D2} = i_{G1} + i_{D1} \quad (7)$$

$$v_{DS2} + v_{GS1} + sL_{int4}i_{D2} + i_{G1}R_{GH} + sL_{int2}i_{G1} = 0 \quad (8)$$

$$R_{SN}i_{SN} + v_{SN} + sL_C i_P + R_{D2}i_P = 0 \quad (9)$$

Where the small signal voltages v_{GS1}, v_{DS1}, v_{DS2} and v_{SN} and small signal currents i_{SN}, i_P, i_{D1} and i_{D2} are defined in Fig. 3b.

During the turn-off transient, the channel current of DHEMT can be considered a step signal [33]. Its small signal i_{H1} is thereby generally modelled as a non-zero small signal [33], [34]. By solving the equations (1)-(9), the V_{DS1} can be obtained as a function of i_{H1}. Given the GaN channel current reduction triggers the turn-off oscillation, i_{H1} is considered as the input of the oscillatory system. Since the voltage oscillation is generated on the DHEMT, the V_{DS1} is considered as the output of the oscillatory system, and the transfer function $H(s)$ can be obtained as:

$$H(s) = \frac{V_{DS1}}{i_{H1}} \quad (10)$$

In this case, $H(s)$ is of the sixth order. The function $H(s)$ is thereby derived numerically by MATLAB.

To obtain the transfer function $H(s)$, the DC operating point should be selected to linearize circuit parameters. In this study, the high-side freewheeling diode is the 650V/26A SiC Schottky diode CVFD20065A. The device under test (DUT) is 650V/20A Transphorm cascode GaN HEMTs TPH3208PS. In

TABLE I
PARAMETERS OF THE SMALL-SIGNAL MODEL.

Symbol	Value	Symbol	Value	Symbol	Value
R_{GH}	0.18 Ω	R_{D2}	0.02 Ω	C_{OSS2}	140 pF
C_{DS1}	35 pF	C_{GD1}	41pF	C_{GS1}	132 pF
L_{DS}	1.2 nH	L_{int2}	0.2 nH	L_{int4}	0.59 nH
L_C	9.8 nH	R_{SN}	6 Ω	C_{SN}	400 pF

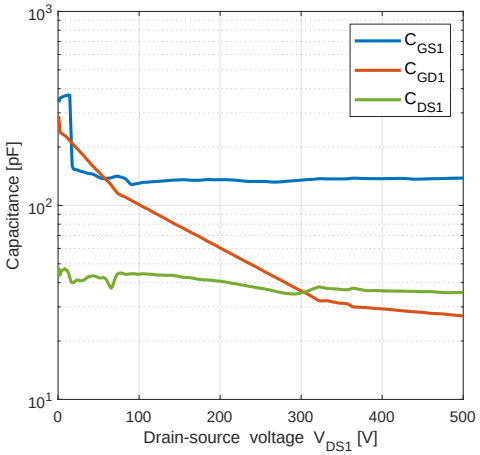

Fig. 4. C-V curve of the GaN DHEMT.

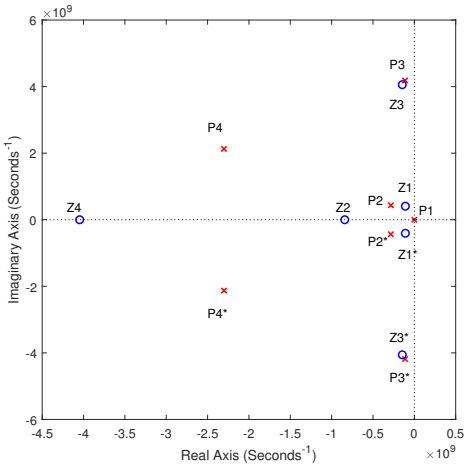

Fig. 5. The poles and zeros of transfer function $H(s)$.

the DUT, a silicon LV MOSFET IRF8707 is utilized to drive a GaN DHEMT [2]. The output stray capacitance C_{OSS2} is linearized at its off-state voltage $V_{DS2(off)}$. The Spice simulation identifies the $V_{DS2(off)}$ is 22V. The C_{OSS2} can thereby be extracted from the C-V curves obtained from the datasheet [35]. In Fig. 4, the C-V curves of GaN DHEMT provided by the device manufacturer are presented. The stray capacitances C_{GD1}, C_{GS1} and C_{DS1} are extracted at $V_{DC}-22V$ based on the C-V curves. The circuit stray inductances are extracted by the Q3D extractor. The internal stray elements like $L_{int1(2,3)}$ and R_{GH} are obtained from the SPICE model provided by the manufacturer. In this section, the RC snubber design $R_{SN}=6\Omega, C_{SN}=400pF$ is used for initial analysis. Various

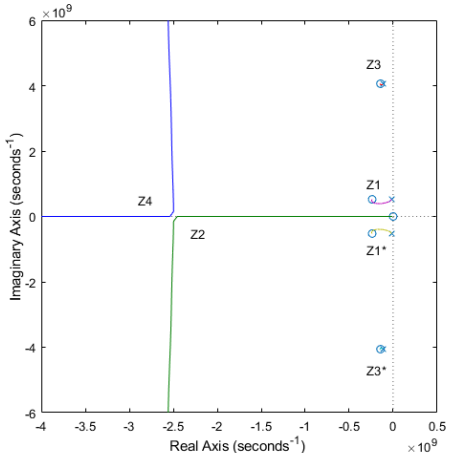

(a) Loci of zeros

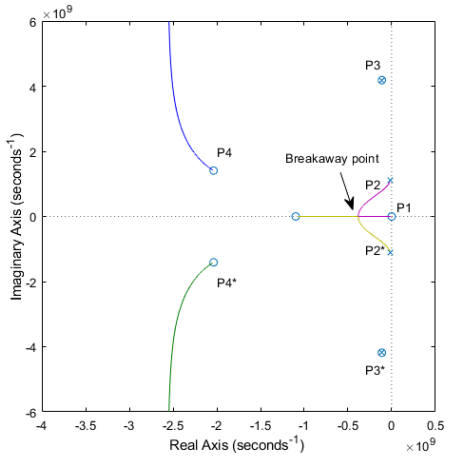

(b) Loci of poles

Fig. 6. Loci of (a) zeros and (b) poles for transfer function $H(s)$ when $R_{SN}=6\Omega$.

RC snubber designs will be utilized in the next few sections to further study the transfer function $H(s)$. The values of all the parameters are summarized in Table I.

IV. ANALYSIS ON THE TRANSFER FUNCTION $H(s)$

Since the system instability is determined by the transfer function $H(s)$, it is necessary to study zeros and poles of $H(s)$ as well as their loci when the snubber resistor and capacitor vary. With the parameters proposed in Table I utilized, the zeros and poles of the transfer function $H(s)$ are first obtained. Fig. 5 shows the zeros and poles of $H(s)$. P_1 is a real pole, whereas P_2, P_2^*, P_3, P_3^*, P_4 and P_4^* are conjugate poles. Z_2 and Z_4 are real zeros, whereas Z_1, Z_1^*, Z_3 and Z_3^* are conjugate zeros. The conjugate poles P_2, P_2^*, P_3 and P_3^* are very close to the imaginary axis and may have a strong impact on system instability. However, the impact of the conjugate poles on the system instability should be further investigated by studying the loci of P_2, P_2^*, P_3, P_3^* P_4 and P_4^*. In the Fig. 5, the conjugate poles P_3 and P_3^* are very close to the conjugate zeros Z_3 and Z_3^*. The P_3, Z_3, P_3^* and Z_3^* can thereby form two pairs of dipoles, which need to be further investigated.

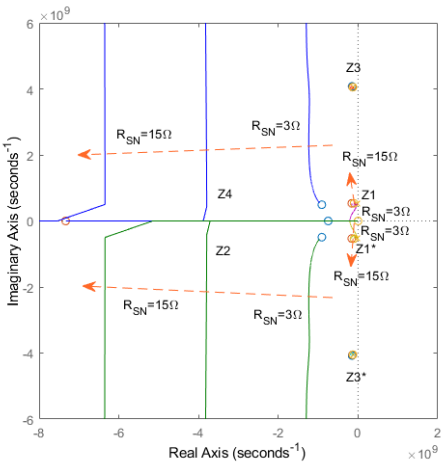

(a) Loci of zeros

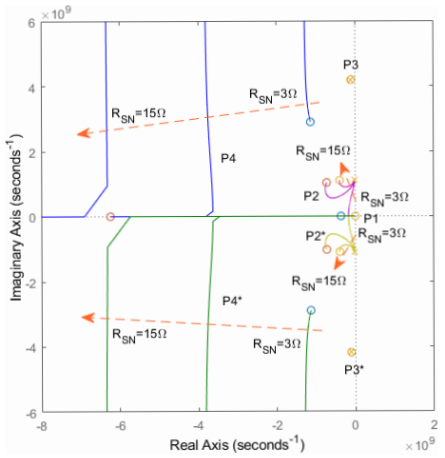

(b) Loci of poles

Fig. 7. Loci of (a) zeros and (b) poles for transfer function $H(s)$ when R_{SN} is 3Ω, 9Ω and 15Ω.

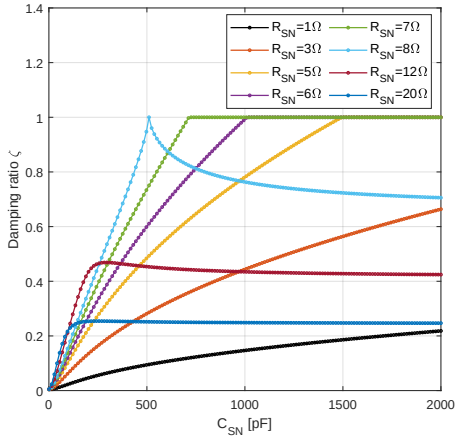

(a) Plot of ζ as a function of C_{SN} with various R_{SN}

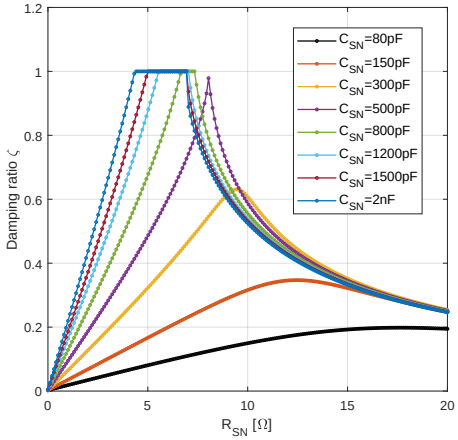

(b) Plot of ζ as a function of R_{SN} with various C_{SN}

Fig. 8. Plot of ζ : (a) ζ as a function of C_{SN} with various R_{SN}; (b) ζ as a function of R_{SN} with various C_{SN}.

Figs. 6a and 6b show the loci of zeros and poles and when $R_{SN} = 6\Omega$ and C_{SN} increases from 10 pF to 20 nF. The P_3, P_3^*, Z_3, and Z_3^* are not moving and thereby can be two pairs of dipoles. With the increase of C_{SN}, P_4 and P_4^* move towards the real axis and their loci are far away from the imaginary axis. P_2 and P_2^* move towards the real axis with the increases of C_{SN}. At the breakaway point, P_2 and P_2^* reach the real axis and the conjugate poles achieves the maximum effective damping ratio.

In Figs. 7a and 7b, the Loci of poles and zeros are plotted when R_{SN} sets to 3Ω, 9Ω and 15Ω while C_{SN} increases from 10 pF to 20 nF. The arrows show the direction of the loci when R_{SN} increases from 3Ω to 15Ω. Based on the plot, the impact of both R_{SN} and C_{SN} on the poles and zeros can be investigated. It can be noticed that P_3, Z_3, P_3^* and Z_3^* approximately stay in the same location despite the variation of C_{SN} and R_{SN}. This confirmed that the P_3, Z_3, P_3^* and Z_3^* are two pairs of dipoles. The impact of P_3 (P_3^*) on the transfer function $H(s)$ is cancelled out by that of the Z_3 (Z_3^*). Therefore, the impact of conjugate poles P_3 and P_3^* on the system instability is neglected.

As shown in Fig 7b, with the increase of R_{SN}, the loci of P_4 and P_4^* greatly move far way from the imaginary axis. Under each R_{SN} value, the P_2, P_2^* are much closer to the imaginary axis than the conjugate poles P_4 and P_4^*. Therefore, the impact of conjugate poles P_4 and P_4^* on the system instability can also be neglected.

With the P_3, P_3^*, P_4 and P_4^* neglected, the poles P_2 and P_2^* become the only conjugate pole pair near the imaginary axis. Therefore, the instability of transfer function $H(s)$ is determined by P_2 and P_2^*. As shown in Figs. 6b and 7b, P_2 and P_2^* can reach to the real axis when R_{SN} is 3Ω and 6Ω. At the breakaway point, P_2 and P_2^* reach the real axis and the oscillatory system achieves the maximum effective damping. However, when R_{SN} is 9Ω and 15Ω, the P_2 and P_2^* can not reach the real axis and the maximum effective damping can not be obtained. Therefore, it is necessary to study the impact of R_{SN} and C_{SN} on P_2 and P_2^* to identify the optimum RC snubber design.

In this study, the damping ratio ζ of P_2 and P_2^* is thereby used to analyse the system instability. ζ can be calculated by:

$$\zeta = \frac{\sigma}{\sqrt{\sigma^2 + \omega^2}} \tag{11}$$

where the -σ and ω are the real and imaginary parts of the conjugate pole pair. When $\zeta > 0$, the oscillatory system is

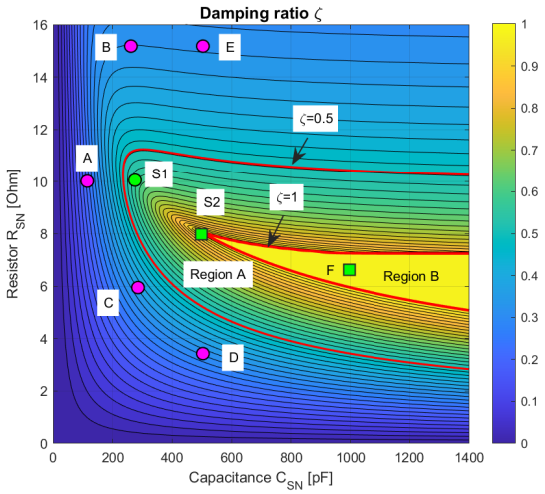

Fig. 9. Contour plot of ζ with the various design points, green squares indicate $\zeta = 1$, green dots indicate $\zeta \in [0.5, 1]$ and purple dots indicate $\zeta < 0.5$.

stable. The maximum effective damping is achieved on the oscillatory system when $\zeta = 1$. By analysing the ζ with various RC snubber designs utilized, the optimum RC snubber design can be investigated, which is proposed in the next section.

V. Optimum Design of RC Snubber

In this section, the impacts of snubber capacitor C_{SN} and snubber resistor R_{SN} on the damping ratio ζ are analysed. Fig. 8a shows the plot of the damping ratio ζ as a function of C_{SN} utilizing various snubber resistances. When $R_{SN} \leq 7\Omega$, ζ rises with the increase of C_{SN} and can achieve the maximum effective damping ratio ($\zeta = 1$) when $R_{SN} \geq 5\Omega$. With the increase of C_{SN}, the energy absorbed on the C_{SN} becomes higher during the oscillatory transient. The energy is dissipated by the snubber resistor R_{SN}, which generates higher effective damping on the oscillatory system. When $R_{SN} \geq 8\Omega$, the ζ increases initially and decrease when C_{SN} is larger than a certain value. The reduction of ζ is due to the impact of C_{SN} on the system instability. A higher C_{SN} can affect the power loop resonance, which makes the oscillatory system more unstable.

Fig. 8b shows the impact of snubber capacitor R_{SN} on the damping ratio ζ with various C_{SN} utilized. With the increase of R_{SN}, the ζ increases initially and reduces in the end. The initial increase of ζ is due to the power dissipation on R_{SN}. With the increase of R_{SN}, a higher power dissipation is generated, which provides a stronger damping effect on the oscillatory system. However, when R_{SN} is large enough, the high impedance in the snubber branch also hinders the conduction of oscillatory current in the snubber circuit. As a result, ζ decreases in the end with the increase of R_{SN}. With larger C_{SN} utilized, the peak value of ζ becomes higher and eventually plateaus at $\zeta = 1$ when $C_{SN} > 500pF$.

Fig. 9 show the contour plot of ζ as a function of R_{SN} and C_{SN}. The contour lines with $\zeta = 1$ and $\zeta = 0.5$ are also marked in the figure. The region which achieves $\zeta = 1$ is plotted in yellow and marked as region B. Within region B,

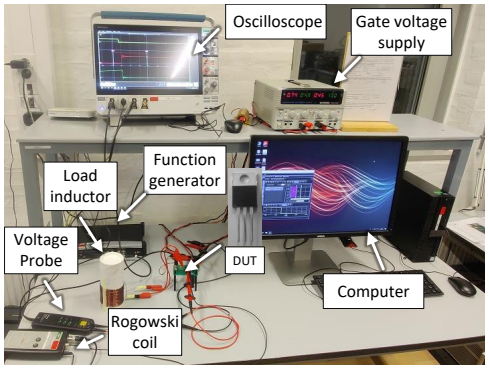

(a) The test platform.

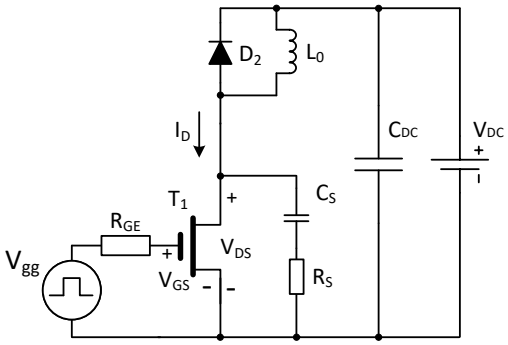

(b) The schematic circuit.

Fig. 10. The double-pulse test setup utilizing RC snubber. (a) Test platform. (b) Schematic of double-pulse test circuit.

the RC snubber design has a maximum damping effect on the turn-off oscillation. However, to achieve $\zeta = 1$, the snubber capacitor C_{SN} have to be pretty large, which can induce high switching losses. According to [23]–[25], the switching oscillation of a wide bandgap device can be satisfactorily damped when the RC snubber design achieves $\zeta > 0.4$. A lower criterion of ζ is thereby used in [23]–[25] to design an RC snubber which can mitigate the switching oscillation without significantly increasing the switching losses. With a safety margin of 0.1, the $\zeta \geq 0.5$ is utilized in this study as a criterion for the RC snubber design. The region with $\zeta \geq 0.5$ is marked as region A, as shown in Fig. 9.

During the switching transient, the snubber capacitor C_{SN} slows down the switching speed and introduces additional power losses [24], [36]. To minimize the power loss increase, the snubber capacitor C_{SN} should be as small as possible. The RC snubber designs with minimum C_{SN} in regions A and B are thereby identified as the optimum RC snubber designs, which are marked as design points S1 and S2 in Fig. 9. The snubber design S1 can provide satisfactorily effective damping with minimized switching losses. Design S2 can achieve maximum effective damping at a cost of higher switching losses. However, with the smallest C_{SN} in region B utilized, the switching loss of design S2 is the lowest among the designs which can achieve $\zeta = 1$.

VI. Experimental Validation

To validate the optimum RC snubber designs, the double-pulse test is performed. Fig. 10 shows the double-pulse test

TABLE II
THE RC SNUBBER DESIGNS UTILIZED IN THE TEST

Snubber design	Resistor R_{SN}	Capacitor C_{SN}
Design S1	10 Ω	300 pF
Design S2	8 Ω	500 pF
Design A	10 Ω	100 pF
Design B	15 Ω	300 pF
Design C	6 Ω	300 pF
Design D	3.5 Ω	500 pF
Design E	15 Ω	500 pF
Design F	6.5 Ω	1000 pF

setup and its equivalent schematic circuit. In the circuit, the low-side DUT T_1 is Transphorm cascode GaN HEMT TPH3208PS. The high-side freewheeling diode D_2 is SiC Schottky diode CVFD20065A. The load inductor $L_0 = 380\mu H$. The external gate resistor $R_{GE} = 27\Omega$. V_{DC} is the DC-bus voltage, which is connected to a power capacitor $C_{DC} = 390\mu F$. The function generator controls a gate driver to generate the gate drive voltage V_{gg}, which switches with 0V/10V. The turn-off oscillation is monitored using drain-source voltage V_{DS}. The V_{DS} waveforms are measured by a high voltage differential probe THDP0200 with a bandwidth of 200 MHz. To obtain the switching energy, the drain current I_D should be measured. To avoid the insertion inductance, a Rogowski coil CWTUM/015/R with a bandwidth of 30 MHz is used to measure the I_D waveforms. With a relatively low bandwidth, the Rogowski coil can not accurately capture the current oscillation but can provide reasonable measurement on the I_D at switching transient. The measured I_D waveforms are thereby only used to calculate the switching energy.

In this study, the test is performed with load current $I_L = 10A$ and DC-bus voltage $V_{DC} = 300V$. Since the I_L does not significant impact on the instability of the switching oscillation [29], $I_L = 10A$ is used since it is the typical load current for the 20A-rated DUTs. The V_{DC} has a significant impact on the insatiability of the switching oscillation. With the increase of V_{DC}, the stray capacitances of the DUTs become smaller. The lower stray capacitances generate reduced effective damping on the oscillatory system, which generates more unstable switching oscillation. When V_{DC} is too low, the switching oscillation is stable and it is impossible to validate the proposed RC snubber design. When V_{DC} is too high, the unstable switching oscillation can cause catastrophic failure, which destroys the DUTs. To validate the RC snubber design without causing catastrophic failure, $V_{DC} = 300V$ is chosen in this study.

In the test, RC snubber designs S1, S2, A, B, C, D, E and F are used, which are marked in Fig. 9. The design points with $\zeta < 0.5$ are marked in purple dots. The green dots indicate the corresponding snubber design has $\zeta \in [0.5, 1]$. The green squares indicate the designs have can achieve maximum damping ratio ($\zeta = 1$). The snubber resistor R_{SN} and snubber capacitor C_{SN} of the RC snubber designs are presented in Table II. The designs S1 and S2 are optimum RC snubber designs, which locates near the far-left boundary of regions A and B, respectively. The other designs A, D, C, D, E and F are introduced to compare with the proposed optimum RC designs.

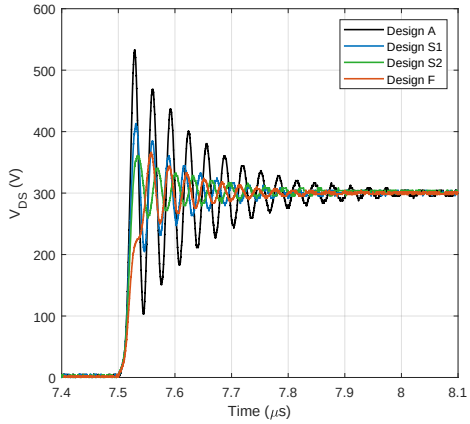

Fig. 11. The experimental turn-off waveforms utilizing the RC snubber designs S1, S2, A and F.

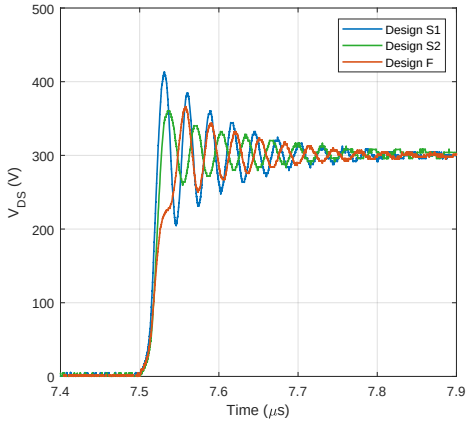

Fig. 12. Zoomed plot of Fig. 11 to compare the RC snubber designs S1, S2 and F.

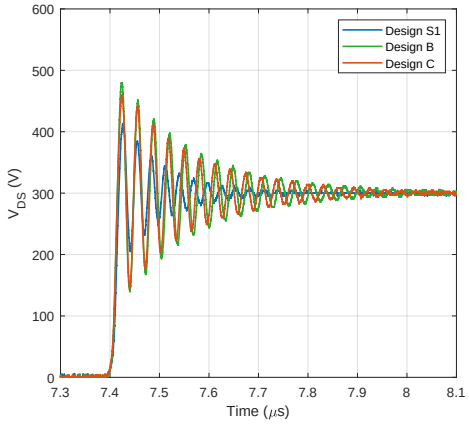

Fig. 13. The experimental turn-off waveforms utilizing the RC snubber designs S1, B and C.

Fig. 11 shows the experimental turn-off waveforms of V_{DS} utilizing RC snubber designs S1, S2, A and F. The RC snubber

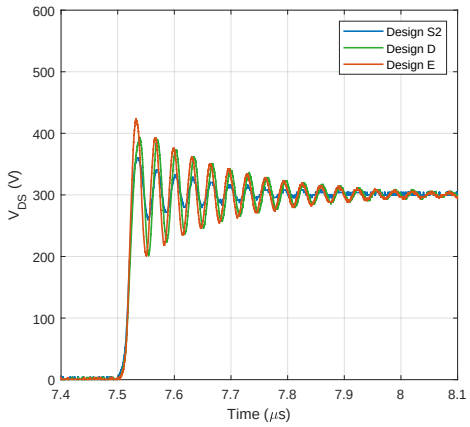

Fig. 14. The experimental turn-off waveforms utilizing the RC snubber designs S2, D and E.

designs A has a damping ratio ζ much smaller than 0.5. The corresponding turn-off oscillation is thereby much more underdamped than the designs S1, S2 and F. With $\zeta > 0.5$, the turn-off oscillation of designs S1, S2 and F receives pretty good effective damping. The test results match with the calculated ζ presented in Fig. 9.

To compare RC snubber designs S1, S2 and F, a zoomed plot of Fig. 11 is shown in Fig. 12. The RC snubber design S2 has a maximum damping ratio $\zeta = 1$, which is significantly larger than that of the design S1, as shown in Fig. 9. The turn-off oscillation of design S2 is thereby significantly damped compared to that of design S1. However, better effective damping comes with a trade-off. The turn-off speed of design S2 is slowed down compared to that of design S1. This gives rise to increased switching losses.

In Fig. 12, the turn-off oscillations of designs S2 and F have similar effective damping. This is because the designs have the same damping ratio ζ ($\zeta = 1$), as shown in Fig. 9. However, due to the much larger C_{SN}, the design F provides a much slower turn-off speed, which gives rise to increased switching losses. The snubber design F is thereby an improper design since it introduced additional switching losses without improvement on the effective damping on the turn-off oscillation.

In Fig. 13, the turn-off oscillations of RC snubber designs S1, B and C are compared. The designs S1, B and C have same $C_{SN} = 300pF$, but different R_{SN} . With 15Ω and 6Ω of R_{SN} utilized, the RC snubber designs B and C thereby have damping ratios much smaller than that of the S1, as shown in Fig. 9. As a result, the turn-off oscillations of RC snubber designs B and C are thereby more underdamped than that of design S1. The test results agree with the calculated ζ presented in Fig. 9.

Fig. 14 shows the turn-off oscillations of RC snubber designs S2, D and E. With the $C_{SN} = 500pF$ utilized, the turn-off oscillations of designs D and E show less damping effect than that of design S2. This is because design S2 has a much higher damping ratio than that of designs D and E, as shown in Fig. 9. The calculated ζ agree with the test results.

In Fig. 12, it can be noticed that the turn-off osculation is not fully suppressed when $\zeta = 1$ is achieved for the oscillatory system. This is because the dV/dt induced false turn-on draws additional energy from the DC-bus voltage V_{DC}. Since the gate loop of DHEMTs is lack of effective damping, the additional energy can support a few oscillatory cycles even when $\zeta = 1$.

VII. Trade-off Relationship between EMI Generation and Turn-off Energy

The switching losses and EMI noise has a trade-off relationship depending on snubber capacitance C_{SN}. With larger C_{SN}, the larger effective damping is achieved at a trade-off of higher switching losses. In this section, the noise-loss trade-off of RC snubber designs S1 and S2 is investigated. To validate that designs S1 and S2 can provide optimum trade-off relationships, designs A and F with different values of C_{SN} are also added for comparison. To obtain the turn-off energy, the drain current I_D is needed. To avoid the insertion inductance in the power loop, a Rogowski coil CWTUM/015/R is used to measure I_D, as shown in Fig. 10. The turn-off energy E_{off} can thereby be obtained by integrating $I_D \times V_{DS}$ during the turn-off transient.

Table III shows the E_{off} of the test waveforms using RC snubber designs S1, S2, A and F. The turn-off energy of the snuberless case are also calculated from the turn-off waveforms presented in Fig. 1b. Compared with the snuberless case, the E_{off} of the designs A and S1 are only a few microjoules higher despite the slowdown of turn-off speed. This is because the designs can greatly suppress the voltages overshoot, which compensates for the turn-off energy increment due to the turn-off speed slowdown. With snubber design S2 utilized, the overshoot voltage can only sightly further reduced compared to that of design S1. The design S2 thereby has a relatively higher turn-off energy increment (10.6 μJ) than the design S1. As shown in Fig. 12, design F has no improvement in the voltage overshoot compared to that of design S2. The E_{off} of design F thereby has a huge increment (61.6 μJ) compared to that of design S2. Following the approach proposed in [37], the V_{DS} voltage spectrum is derived by fast Fourier transformation (FFT) of the experimental waveforms of V_{DS}. Fig 15 compares the V_{DS} spectra for the RC snubber designs S1, S2, A and F. Due to the underdamped turn-off oscillation, a spectrum peak is observed on the voltage spectrum of design A in the region A (around 30-40 MHz). Compared to design A, the spectrum peak reduces by 7.3 dB when snubber design S1 is used. For design S2, the spectrum peak further reduces by 2.4 dB. The spectrum peak of design F is similar to that of design S2 since they have the same damping ratio for the turn-off oscillation. In region B (around 10-20 MHz), the spectrum amplitude of design F is lower than that of design S2. However, this is due to the reduced dV/dt, not the turn-off oscillation.

From the analysis presented above, it can be concluded that snubber designs S1 and S2 can provide a better noise-loss trade-off compared to the other designs. The design S1 greatly reduces the spectrum peak by 7.3 dB at a cost of 8.4 μJ of additional turn-off energy. The design S2 can further

TABLE III
THE TURN-OFF ENERGY E_{off} OF VARIOUS RC SNUBBER DESIGNS

Snubber design	R_{SN}	C_{SN}	E_{off}
Snuberless	-	-	52.5 μJ
Design A	10 Ω	100pF	57.7 μJ
Design S1	10 Ω	300pF	60.9 μJ
Design S2	8 Ω	500pF	71.5 μJ
Design F	6.5Ω	1000pF	133.1 μJ

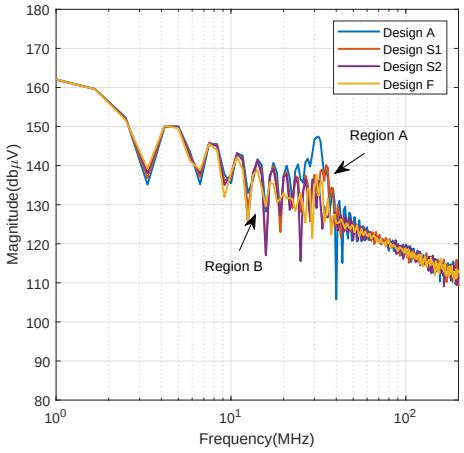

Fig. 15. Spectra of V_{DS} for the RC snubber designs A, B, C and D.

reduce spectrum peak by 2.4 dB at a relatively higher turn-off energy increment of 19 μJ. However, the design S2 is still a good choice for applications which require maximum reduction of the EMI noise. Design A has a high spectrum peak due to the underdamped turn-off oscillation. Design F greatly increases the turn-off energy without significantly improving the spectrum peak in region A compared to the design S2. Therefore, they are bad choices for the RC snubber design.

VIII. Conclusion

This paper presents an optimum RC snubber design method to suppress the turn-off oscillation of cascode GaN HEMTs. The major contribution of the paper can be summarized as follows:

1. The turn-off oscillation of cascode GaN HEMTs is mainly generated by the resonance between the underdamped internal gate loop of GaN DHEMT and power loop. To design an RC snubber which can suppress the resonant, the transfer function $H(s)$ of the oscillatory system is derived to describe the instability of the oscillation.

2. The analysis on the $H(s)$ shows the instability of the oscillation is determined by a conjugate pole pair P_2 and P_2^*. Based on the analyses on the damping ratio ζ of the pole pair, the RC snubber design regions which can achieve $\zeta > 0.5$ and $\zeta = 1$ are identified to design the RC snubber.

3. The introduction of the RC snubber slows down the switching speed and generates additional power losses. To minimize the power losses, two optimum RC snubber designs S1 and S2, which can provide the best noise-loss trade-off, are proposed. The design S1 can satisfactorily suppress the turn-off oscillation with minimum power energy. The design S2 can provide maximum effective damping on the oscillation at a cost of an increased turn-off energy. However, the turn-off energy increment is the smallest among the RC snubber designs that can provide maximum effective damping.

4. In the end, the test is performed to validate the proposed RC snubber design method. The alignment of experimental turn-off oscillation waveforms and the analytical results validate the proposed design methods. The experimental investigation on the V_{DS} voltage spectra and turn-off energy also proves that the proposed designs S1 and S2 can provide the best noise-loss trade-off.

IX. Data Availability Statement

The data that support the findings of this study are available from the corresponding author upon reasonable request.

X. Acknowledgement

This work was supported by the Independent Research Fund Denmark (DFF) through the CLEAN-Power Project at the Department of Energy, Aalborg University, Aalborg, Denmark.

References

[1] Jones, E.A., Wang, F.F., Costinett, D.: 'Review of commercial GaN power devices and GaN-based converter design challenges', *IEEE Journal of Emerging and Selected Topics in Power Electronics*, 2016, **4**, (3), pp. 707–719

[2] Xue, P., Iannuzzo, F.: 'Self-sustained Turn-off Oscillation of Cascode GaN HEMTs: Occurrence Mechanism, Instability Analysis and Oscillation Suppression', *IEEE Transactions on Power Electronics*, 2021,

[3] Siemieniec, R., Nöbauer, G., Domes, D.: 'Stability and performance analysis of a sic-based cascode switch and an alternative solution', *Microelectronics Reliability*, 2012, **52**, (3), pp. 509–518

[4] Huang, X., Du, W., Lee, F.C., Li, Q., Zhang, W.: 'Avoiding divergent oscillation of a cascode GaN device under high-current turn-off condition', *IEEE Transactions on Power Electronics*, 2017, **32**, (1), pp. 593–601

[5] Xu, Z., Zhang, W., Xu, F., Wang, F., Tolbert, L.M., Blalock, B.J. 'Investigation of 600 V GaN HEMTs for high efficiency and high temperature applications'. In: Applied Power Electronics Conference and Exposition. (, 2014. pp. 131–136

[6] He, L., Xuan, Z., Wen, L., Brothers, J.A., Jin, W.: 'Paralleled operation of high voltage Cascode GaN HEMTs', *IEEE Journal of Emerging & Selected Topics in Power Electronics*, 2017, **4**, (3), pp. 815–823

[7] Zhang, W., Huang, X., Lee, F.C., Li, Q. 'Gate drive design considerations for high voltage cascode GaN HEMT'. In: IEEE Applied Power Electronics Conference and Exposition. (, 2014. pp. 1484–1489

[8] Lemmon, A., Mazzola, M., Gafford, J.: 'Instability in half-bridge circuits switched with wide band-gap transistors', *IEEE Transactions on Power Electronics*, , **29**, (5), pp. 2380–2392. DOI: 10.1109/TPEL.2013.2273275

[9] Xue, P., Maresca, L., Riccio, M., Breglio, G., Irace, A.: 'Self-sustained turn-off oscillation of SiC MOSFETs: Origin, instability analysis, and prevention', *Energies*, 2019, **12**, (11), pp. 2211

[10] Xue, P., Maresca, L., Riccio, M., Breglio, G., Irace, A.: 'Analysis on the Self-Sustained Oscillation of SiC MOSFET Body Diode', *IEEE Transactions on Electron Devices*, 2019, **66**, (10), pp. 4287–4295

[11] Xue, P., Maresca, L., Riccio, M., Breglio, G., Irace, A.: 'Investigation on the short-circuit oscillation of cascode GaN HEMTs', *IEEE Transactions on Power Electronics*, 2019, **35**, (6), pp. 6292–6300

[12] Zhang, B., Wang, S.: 'A survey of EMI research in power electronics systems with wide-bandgap semiconductor devices', *IEEE Journal of Emerging and Selected Topics in Power Electronics*, 2019, **8**, (1), pp. 626–643

[13] Liu, T., Wong, T.T., Shen, Z.J.: 'A survey on switching oscillations in power converters', *IEEE Journal of Emerging and Selected Topics in Power Electronics*, 2019, **8**, (1), pp. 893–908

[14] Ryo, T., Takamasa, A., Bernhard, H., Michael, Z., Mike, H.: 'Cascode GaN FET Dynamic Characterization', *Bodo's Power Systems*, Mar. 2021, pp. 34–37

[15] Xue, P., Maresca, L., Riccio, M., Breglio, G., Irace, A.: 'Experimental study on the short-circuit instability of cascode GaN HEMTs', *IEEE Transactions on Electron Devices*, 2020, **67**, (4), pp. 1686–1692

[16] Zan, H., Jason, C.. 'Recommended external circuitry for transphorm GaN FETs'. (, 2016

[17] Zhu, T., Zhuo, F., Zhao, F., Wang, F., Zhao, T.: 'Quantitative model-based false turn-on evaluation and suppression for cascode GaN devices in half-bridge applications', *IEEE Transactions on Power Electronics*, 2019, **34**, (10), pp. 10166–10179

[18] Zhao, F., Li, Y., Chen, Z., Yang, S., Chen, J.: 'Negative Conductance Modeling and Stability Analysis of High-Frequency Oscillation Based on Cascode GaN Circuits', *IEEE Access*, 2020, **8**, pp. 114100–114111

[19] Xue, P., Iannuzzo, F.: 'Ferrite beads design to improve turn-off characteristics of cascode gan hemts: An optimum design method', *IEEE Journal of Emerging and Selected Topics in Power Electronics*, 2023, **11**, (3), pp. 3184–3194

[20] Joko, M., Goto, A., Hasegawa, M., Miyahara, S., Murakami, H. 'Snubber circuit to suppress the voltage ringing for SiC device'. In: Proceedings of PCIM Europe. (VDE, 2015. pp. 1–6

[21] Yatsugi, K., Nomura, K., Hattori, Y.: 'Analytical technique for designing an RC snubber circuit for ringing suppression in a phase-leg configuration', *IEEE Transactions on Power Electronics*, 2017, **33**, (6), pp. 4736–4745

[22] Torsæter, B.N., Tiwari, S., Lund, R., Midtgård, O.M. 'Experimental evaluation of switching characteristics, switching losses and snubber design for a full sic half-bridge power module'. In: International Symposium on Power Electronics for Distributed Generation Systems (PEDG). (, 2016. pp. 1–8

[23] Chen, J., Luo, Q., Huang, J., He, Q., Sun, P., Du, X.: 'Analysis and design of an RC snubber circuit to suppress false triggering oscillation for GaN devices in half-bridge circuits', *IEEE Transactions on Power Electronics*, 2019, **35**, (3), pp. 2690–2704

[24] Xu, M., Yang, X., Li, J.: 'C-RC Snubber Optimization Design for Improving Switching Characteristics of SiC MOSFET', *IEEE Transactions on Power Electronics*, 2022,

[25] Chen, J., Luo, Q., Wei, Y., Zhang, X., Du, X.: 'The sustained oscillation modeling and its quantitative suppression methodology for GaN devices', *IEEE Transactions on Power Electronics*, 2020, **36**, (7), pp. 7927–7941

[26] Liu, T., Ning, R., Wong, T.T., Shen, Z.J.: 'Modeling and analysis of SiC MOSFET switching oscillations', *IEEE Journal of Emerging and Selected Topics in Power Electronics*, 2016, **4**, (3), pp. 747–756

[27] Yang, X., Xu, M., Li, Q., Wang, Z., He, M.: 'Analytical method for rc snubber optimization design to eliminate switching oscillations of sic mosfet', *IEEE Transactions on Power Electronics*, 2021,

[28] Wu, Y., Yin, S., Li, H., Ma, W.: 'Impact of RC Snubber on Switching Oscillation Damping of SiC MOSFET With Analytical Model', *IEEE Journal of Emerging and Selected Topics in Power Electronics*, 2019, **8**, (1), pp. 163–178

[29] Wang, K., Yang, X., Wang, L., Jain, P.: 'Instability analysis and oscillation suppression of enhancement-mode gan devices in half-bridge circuits', *IEEE Transactions on Power Electronics*, 2018, **33**, (2), pp. 1585–1596

[30] Luo, B., Luo, G., Li, S.: 'An integrated modelling and parameter design method for the rc snubber in novel cascode gan-based bridge convertors', *IET Power Electronics*, 2022, **15**, (14), pp. 1451–1467

[31] Lyu, G., Wang, Y., Wei, J., Zheng, Z., Chen, K.J.: 'Dv/Dt-control of 1200-V normally-off SiC-JFET/GaN-HEMT cascode device', *IEEE Transactions on Power Electronics*, 2020, **36**, (3), pp. 3312–3322

[32] Aggeler, D., Canales, F., Biela, J., Kolar, J.W.: 'Dv/Dt-Control Methods for the SiC JFET/Si MOSFET Cascode', *IEEE Transactions on Power Electronics*, 2012, **28**, (8), pp. 4074–4082

[33] Milady, S., Silber, D., Pfirsch, F., Niedernostheide, F.J. 'Simulation studies and modeling of Short Circuit current oscillations in IGBTs'. In: International Symposium on Power Semiconductor Devices & Ics. (, 2009. pp. 37–40

[34] Milady, S.: 'Spatial and temporal instabilities in high voltage power devices', , 2010,

[35] International Rectifier. 'IRF8707 Power MOSFET Datasheet'. (, 2007. Available: http:/www.irf.com

[36] Rosseti, N., Lan, R. 'Correct snubber power loss estimate saves the day'. In: Design Solutions. (, 2016. pp. 1–3

[37] Costa, F., Magnon, D.: 'Graphical analysis of the spectra of EMI sources in power electronics', *IEEE Transactions on Power Electronics*, 2005, **20**, (6), pp. 1491–1498